

# ATLASGAL — Compact source catalogue: $330^\circ < \ell < 21^\circ$ \*

Y. Contreras<sup>1,2\*\*</sup>, F. Schuller<sup>1,3</sup>, J. S. Urquhart<sup>1</sup>, T. Csengeri<sup>1</sup>, F. Wyrowski<sup>1</sup>, H. Beuther<sup>4</sup>, S. Bontemps<sup>5</sup>, L. Bronfman<sup>2</sup>,  
T. Henning<sup>4</sup>, K. M. Menten<sup>1</sup>, P. Schilke<sup>6</sup>, C. M. Walmsley<sup>7,8</sup>, M. Wienen<sup>1</sup>, J. Tackenberg<sup>4</sup>, H. Linz<sup>4</sup>

<sup>1</sup> Max-Planck-Institut für Radioastronomie, Auf dem Hügel 69, Bonn, Germany

<sup>2</sup> Departamento de Astronomía, Universidad de Chile, Casilla 36-D, Santiago, Chile

<sup>3</sup> European Southern Observatory, Alonso de Cordova 3107, Vitacura, Santiago, Chile

<sup>4</sup> Max-Planck-Institut für Astronomie, Königstuhl 17, 69117 Heidelberg, Germany

<sup>5</sup> Laboratoire d'Astrophysique de Bordeaux - UMR 5804, CNRS Université Bordeaux 1, BP 89, 33270 Floirac, France

<sup>6</sup> I. Physikalisches Institut, Universität zu Köln, Zùlpicher Str. 77, 50937 Köln, Germany

<sup>7</sup> Osservatorio Astrofisico di Arcetri, Largo E. Fermi, 5, 50125 Firenze, Italy

<sup>8</sup> Dublin Institute for Advanced Studies, Burlington Road 10, Dublin 4, Ireland

Received xxx; accepted xxx

## ABSTRACT

**Context.** The APEX Telescope Large Area Survey of the Galaxy (ATLASGAL) is the first systematic survey of the inner Galactic plane in the sub-millimetre. The observations were carried out with the Large APEX Bolometer Camera (LABOCA), an array of 295 bolometers observing at  $870\ \mu\text{m}$  (345 GHz).

**Aims.** Here we present a first version of the compact source catalogue extracted from this survey. This catalogue provides an unbiased database of dusty clumps in the inner Galaxy.

**Methods.** The construction of this catalogue was made using the source extraction routine SExtractor. We have cross-associated the obtained sources with the IRAS and MSX catalogues, in order to constrain their nature.

**Results.** We have detected 6639 compact sources in the range from  $330 \leq \ell \leq 21$  degrees and  $|b| \leq 1.5$  degrees. The catalogue has a 99% completeness for sources with a peak flux above  $6\sigma$ , which corresponds to a flux density of  $\sim 0.4\ \text{Jy beam}^{-1}$ . The parameters extracted for sources with peak fluxes below the  $6\sigma$  completeness threshold should be used with caution. Tests on simulated data find the uncertainty in the flux measurement to be  $\sim 12\%$ , however, in more complex regions the flux values can be overestimated by a factor of 2 due to the additional background emission. Using a search radius of  $30''$  we found that 40% of ATLASGAL compact sources are associated with an IRAS or MSX point source, but,  $\sim 50\%$  are found to be associated with MSX  $21\ \mu\text{m}$  fluxes above the local background level, which is probably a lower limit to the actual number of sources associated with star formation.

**Conclusions.** Although infrared emission is found towards the majority of the clumps detected, this catalogue is still likely to include a significant number of clumps that are devoid of star formation activity and therefore excellent candidates for objects in the coldest, earliest stages of (high-mass) star formation.

**Key words.** Stars: formation – Surveys – Submillimeter – Catalogues

## 1. Introduction

The processes and time scales involved in the formation of high-mass stars are still poorly understood, although such stars play an important role in the evolution of their parental clouds and the subsequent star formation inside them (Krumholz & Bonnell, 2007). Moreover, they interact with their environment injecting an enormous amount of energy both radiative and mechanical (Hoare & Franco, 2007).

Great advances have been made in understanding how low-mass stars form (McKee & Ostriker, 2007), but the situation for high-mass stars is still very unclear. Different scenarios have been proposed that provide a theoretical framework for the formation of high-mass stars such as competitive accretion (Bonnell et al., 2004) and core accretion (McKee & Tan, 2003). On the observational side, the short time scales (McKee & Tan,

2002) involved in the different stages of the formation process make it difficult to build large representative samples for the statistical studies necessary to robustly test these theories.

Several surveys have been carried out to study the environments of high-mass star-forming regions. The drawback of many of these surveys is that they target samples that fulfil certain selection criteria (e.g. maser emission, or peculiar far-infrared colours), and, as such, they are biased towards given evolutionary stages (see e.g. Wyrowski, 2008). For example, methanol masers have been found to be exclusively associated with the very early stages of high-mass star formation up to the more evolved ultracompact HII region phase and were the subject of the recent methanol multibeam (MMB; Green et al. 2009) survey. The Red MSX Source survey (RMS; Urquhart et al. 2008) targets high-mass young stellar objects (MYSOs) that are known to be mid-infrared bright, while the Co-Ordinated Radio and Infrared Source for High-Mass Star Formation (CORNISH; Hoare et al. 2012) targets the ultra-compact (UC) HII region stage at which point the young embedded star begins to ionize its surrounding envelope and hence represents a later evolutionary stage.

\* The full catalogue and the calibrated emission maps are only available in electronic form at the CDS via anonymous ftp to cdsarc.u-strasbg.fr (130.79.125.5) or via <http://cdsweb.u-strasbg.fr/cgi-bin/qcat?J/A+A/>.

\*\* Current address: CSIRO Astronomy and Space Science, P.O. Box 76, Epping NSW 1710, Australia. e-mail: yanett@das.uchile.cl

All of these surveys provide useful statistics on the particular stage targeted (an evolutionary snapshot) but do not provide a complete overview of high-mass star formation. What is needed is a Galaxy wide survey using an unbiased tracer that links all of these complementary surveys together. The ideal tracer to choose is the submillimetre thermal emission from dust as it is optically thin, and so traces the whole column of material across the Galaxy, and is associated with all stages of high-mass star formation. However, until recently, limitations in mapping speeds have resulted in limited coverage of the Galactic plane. For example, SCUBAs<sup>1</sup> 9-year lifetime, a total area of only 29.3 deg<sup>2</sup> has been surveyed at 850  $\mu\text{m}$  (Di Francesco, 2008).

The need for unbiased surveys to get a complete census of the regions where high-mass stars are being formed has led to several projects to map the Galactic plane at millimetre and submillimetre wavelengths. The APEX<sup>2</sup> Telescope Large Area Survey of the Galaxy (ATLASGAL; Schuller et al., 2009) is the first complete survey of the inner Galactic plane providing an unbiased view and complete census of high-mass star-forming cores and clumps. It is well complemented by the Herschel Infrared Galactic plane (Hi-GAL; Molinari et al., 2010) survey in the far-infrared range at a similar high spatial resolution of  $\sim 20''$  (e.g., 0.5 pc at 5 kpc), and at slightly longer wavelengths with the Bolocam Galactic Plane Survey (BGPS; Aguirre et al., 2011). Sub-mm surveys, as opposed to other surveys at shorter wavelengths such as the Galactic Legacy Infrared Mid-Plane Survey Extraordinaire (GLIMPSE Benjamin et al., 2003) or the MIPS Inner Galactic Plane Survey (MIPSGAL; Carey et al., 2009), are sensitive to dust in a broad range of temperatures, including the coldest dust. Therefore, such surveys have the potential to trace the earliest stages of star formation.

In this paper, we present a compact source catalogue extracted from a limited range of the ATLASGAL survey. ATLASGAL is an unbiased survey of the Galactic plane at 870  $\mu\text{m}$  with LABOCA (Large APEX Bolometer Camera; Siringo et al., 2009), and is the largest and most sensitive ground-based sub-mm survey to date. The catalogue presented here is extracted from a subset of the data collected from 2007 to 2010, which covered 153 deg<sup>2</sup>, about one third of the total survey area (420 deg<sup>2</sup>). A catalogue will be compiled from the remaining fields and be published in a companion paper when the data reduction and analysis of these fields has been completed.

The aim of this survey is to obtain a complete census of cold dusty clumps in the Galaxy, and to study their distribution across the Galaxy. This survey reveals a complete sample of different stages of high-mass star formation. It will be complementary to the other Galactic plane surveys such as UKIDSS (Lawrence et al. 2007) and VISTA Variables in the Via Lactea (VVV; Saito et al. 2012) at the near-infrared; GLIMPSE and MIPSGAL at the mid- to far-infrared (Benjamin et al. 2003 and Carey et al. 2009 respectively); Hi-GAL which spans the far-infrared and sub-millimetre wavelengths (70-500  $\mu\text{m}$ ; Molinari et al. 2010) between MIPSGAL and ATLASGAL; and finally the 5 GHz CORNISH Survey. These surveys combined together will provide a complete wavelength coverage of the Galactic plane from the near-infrared to the radio, and will also form a unique database for follow-up observations.

To demonstrate the potential impact of this unique database, the ATLASGAL data has been used in numerous studies; Wielen et al. (2012) determined the temperatures and kinematic distances of  $\sim 1000$  clumps in various evolutionary stages using ammonia follow-up observations;  $\sim 1500$  ATLASGAL sources are part of the MALT90 project (Foster et al., 2011)<sup>3</sup>, which simultaneously maps these sources in 16 spectral lines in the 3-mm wavelength range with the Mopra radio telescope; Deharveng et al. (2010) studied the association of infrared bubbles with ATLASGAL dust clumps; and based on ATLASGAL data Tackenberg et al. (2012) identified a number of starless cores, using indicators of star formation in GLIMPSE and MIPSGAL images.

In Sect. 2, we describe the observations, and in Sect. 3 we detail how the sources were extracted. Tests on the reliability of the extraction algorithm are described in Sect. 4. In Sect. 5 we present the compact source catalogue and discuss the distributions of the various source parameters, while in Sect. 6 we investigate the correlation of ATLASGAL sources with the IRAS and MSX source catalogues and with other types of objects. Finally, we summarise our results in Sect. 7.

## 2. Observations

The observations were carried out with LABOCA (Siringo et al., 2009) at the APEX (Atacama Pathfinder EXperiment) 12 m submillimetre antenna (Güsten et al., 2006), located in Llano de Chajnantor, Chile. The typical pointing r.m.s. error was measured to be  $\sim 4''$ . The bandpass of LABOCA is centred at 345 GHz, with a bandwidth of 60 GHz. At this frequency, the APEX beam FWHM is  $19''.2$ .

In the present paper, we will focus on the region  $330^\circ \leq \ell \leq 21^\circ$ ,  $-1.5^\circ \leq b \leq 1.5^\circ$  (153 deg<sup>2</sup>). Future versions of the catalogue will cover the full 420 deg<sup>2</sup> observed as part of ATLASGAL.

The observations were made using on-the-fly maps with a scanning velocity of 3'/s. They produced slices of 1° width in Galactic longitude times 2° length in Galactic latitude for the observations carried out during 2007 and slices of 1° in Galactic longitude times 2 to 3° in Galactic latitude during 2008 to 2010. To avoid artefacts inherent to the observing technique, each position in the sky is covered at least twice, in two or more maps observed with different scanning angles. The flux calibration was made using planets as primary calibrators (Mars, Neptune and Uranus), and secondary calibrators (bright Galactic sources with known fluxes from the commissioning of LABOCA). The errors in peak flux are estimated to be lower than 15% (Schuller et al., 2009).

The data reduction was made using the BOLometer array data Analysis package (BoA; Schuller, 2012). The steps involved in the data reduction are explained in detail in Schuller et al. (2009), and can be summarised as: flagging bad bolometers, removing the correlated noise, flagging noisy bolometers, despiking, low frequency filtering, and subtracting a first order baseline. The maps are then built by co-adding the signals from all bolometers, using a weighted mean with natural weighting. A weight map is also calculated from the sum of all the weights that contribute to each pixel in the final map. An r.m.s. map can then be computed as  $1/\sqrt{\text{weight}}$ .

A problem inherent to the reduction of ground-based bolometer data is the loss of the extended emission, which is filtered out when the correlated noise is subtracted. As a result, uniform

<sup>1</sup> Submillimeter Common User Bolometer Array, (Holland et al., 1999)

<sup>2</sup> This publication is based on data acquired with the Atacama Pathfinder Experiment (APEX) is a collaboration between the Max-Planck-Institut für Radioastronomie, the European Southern Observatory, and the Onsala Space Observatory.

<sup>3</sup> <http://malt90.bu.edu/>

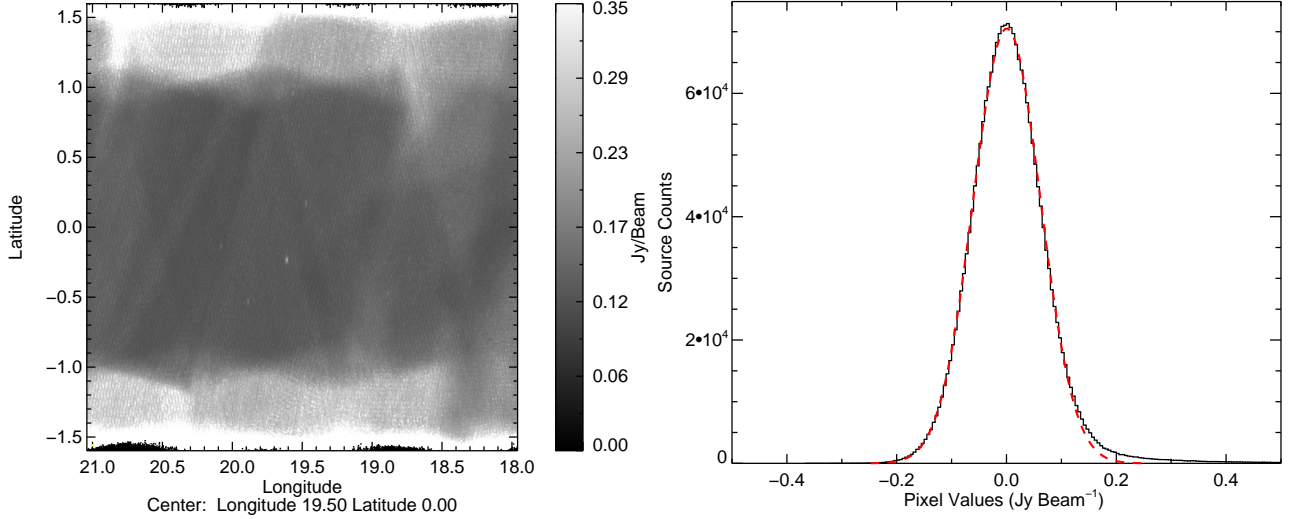


**Fig. 1.** In the left panel we present an r.m.s. noise map of a  $3^\circ \times 3^\circ$  field centred on  $\ell = 19.5^\circ$  and  $b = 0$  showing how the noise varies as a function of Galactic longitude and latitude. In the right panel we present a histogram of the pixel values found within  $|b| < 1^\circ$  where the noise is approximately constant. The red line shows the result of a Gaussian fit to the noise, from which we estimate the average noise for this field ( $\sigma_{\text{r.m.s.}} \simeq 60 \text{ mJy}$ ).

emission at angular scales larger than  $2.5''$  is removed. This reduction scheme was optimised to recover compact sources. The final maps are built with a pixel size of  $6''$ , corresponding to a  $\sim 1/3$  of the telescope beam. The size of each map is of  $3 \times 3$  degree, having an overlap between two consecutive maps of  $\sim 4.5$  arc minutes.

In the left panel of Fig. 1 we present an example of a final noise map, i. e. the r.m.s. noise level distribution over a reduced map. As can be seen from this map the noise is reasonably uniform within  $|b| < 1^\circ$ , however, due to poorer coverage at higher latitude ( $|b| > 1^\circ$ ) the pixel to pixel r.m.s. is significantly larger, typically  $150\text{--}250 \text{ mJy beam}^{-1}$ . The vast majority of the emission seen in the ATLASGAL maps is concentrated close to the Galactic mid-plane and so the sensitivity of the survey can be considered fairly uniform. In the right panel of Fig. 1 we present a histogram of the flux values of pixels with  $|b| < 1^\circ$ . The r.m.s. noise is well modelled by a Gaussian fit (shown as a dashed red line), from which we estimate the r.m.s. noise to be  $\sim 60 \text{ mJy beam}^{-1}$ . We estimate the r.m.s. noise in each field in the same way and present a plot showing how the noise varies as a function of Galactic longitude in Fig. 2. This plot reveals that the noise is fairly uniform for the regions presented here ( $\sim 50\text{--}70 \text{ mJy beam}^{-1}$ ), with the observed variations resulting from different weather conditions and elevation of the various observations. This is particularly noticeable for the maps within  $+7$  and  $+17$  degrees where the higher noise in these maps is believed to be due to a combination of high airmass and poorer weather conditions.

### 3. Source extraction

To create the compact source catalogue we used the source extraction algorithm SExtractor (Bertin & Arnouts, 1996). Although SExtractor was originally created as a method of source extraction for visible and infrared images, it has been used with good results for the extraction of sub-mm sources as well by Thompson et al. (2006) and more recently by the *Planck* team to produce the higher frequency components of their com-

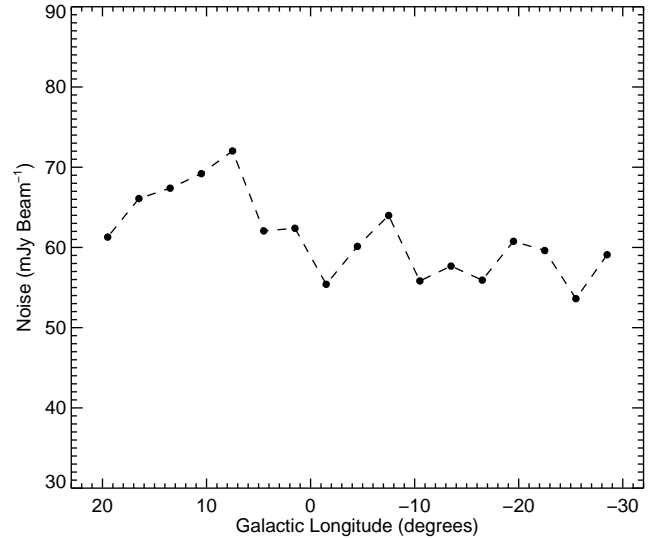


**Fig. 2.** Plot showing how the noise varies as a function of Galactic longitude. The points show the standard deviation of the pixel to pixel variation averaged for each  $3^\circ \times 3^\circ$  field, however, we have only included pixels with  $|b| < 1^\circ$  where the noise is relatively uniform and where the vast majority of the  $870 \mu\text{m}$  emission is concentrated. A dashed line connects the points to emphasize the field-by-field variations in the noise.

compact source catalogue (217–857 GHz; Planck Collaboration et al. 2011).

Most source extraction algorithms assume that the noise level is constant across the emission map supplied. However, in most surveys this is unlikely to be the case due to variations in coverage, weather, elevation and instrumental effects, which make the noise level vary across the field, and this is indeed the case for the ATLASGAL survey. In Fig. 1 we present the noise

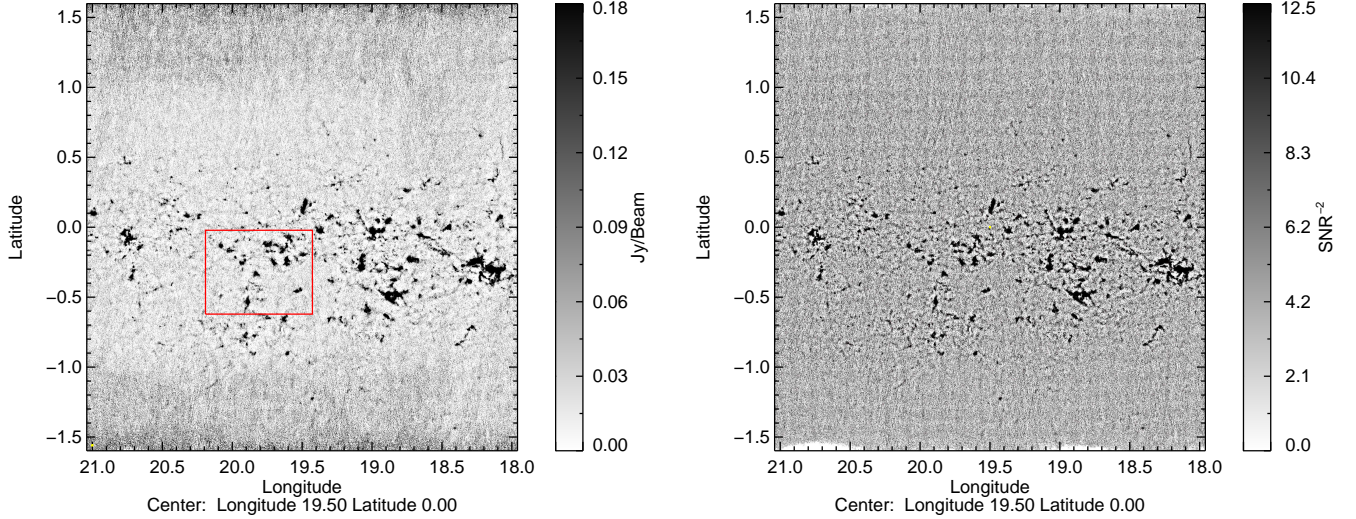


**Fig. 3.** Example of an ATLASGAL emission map (left panel) and the corresponding filtered signal-to-noise ratio map (see text for details). The region outlined in red indicates the field presented in Fig. 4.

map for the  $3^\circ \times 3^\circ$  field centred on  $\ell = 19.5^\circ$  and  $b = 0$ . The fact that most source extraction algorithms assume a constant noise can lead to real sources lying in areas of lower than average noise regions being missed, while conversely, in higher noise regions there is a danger that spurious noise spikes will be mistakenly interpreted as real sources.

In order to reduce the number of spurious sources and avoid missing genuine sources we have converted each emission map into a signal-to-noise ratio map by dividing it by its corresponding noise map. These maps also contain a large fraction of low surface brightness diffuse and filamentary emission, particularly towards the Galactic centre and towards the tangent with the Norma spiral arm and other prominent star forming regions. This not only complicates the identification of compact sources but can also lead to the identification of a large number of spurious sources. To limit the source confusion due to large scale extended diffuse emission we have removed it using the program `FINDBACK`, which is part of the `CUPID`<sup>4</sup> clump identification and analysis package. This produces maps with a higher contrast between compact sources and their local background. In Fig. 3 we present an emission map to show the affect of the varying noise level in the left panel, while in the right panel we show the same map after smoothing the variations by dividing through by the noise map and spatial filtering to remove the diffuse background. These two images nicely illustrate the advantages of using the signal-to-noise map for the source detection.

To summarise, we first smoothed the noise variations by dividing the maps by the noise map and created a signal-to-noise map, and as a second step we applied spatial filtering to remove part of the extended emission. This is compared to the original maps with varying noise level in Fig. 3.

`SExtractor` can work on two images simultaneously, one for the source detection and one for measuring the physical parameters of each source. We have used the spatially filtered signal-to-noise map for source detection, however, we have used the original emission maps to extract the corresponding source parameters. In this way, the flux and size of the sources are not

affected by the filtering process performed for the source detection. These steps should ensure that only genuine sources make it into the final catalogue. In Fig. 4 we present a subregion, taken from the emission map presented in the left panel of Fig. 3, showing the positions and sizes of sources identified by `SExtractor`.

The ATLASGAL maps were searched for emission above a threshold of  $3\sigma_{\text{r.m.s.}}$ , where  $\sigma_{\text{r.m.s.}}$  is the local noise level determined from a user defined box by `SExtractor`. The value of this threshold was determined empirically by varying its value for a number of test regions so as to optimise the number of genuine sources detected while avoiding the inclusion of the more dubious sources. In addition to the threshold we also reject any sources with fewer pixels than the beam integral (i.e.,  $\sim 11$  pixels).

To separate possible blended sources, `SExtractor` divided the emission into 40 sub-levels of flux. In each of these 40 levels, the ratio of the integrated intensities of adjacent pixels is computed. If the ratio between two pixels is greater than 0.001, then those pixels are considered part of a different source. If not, both pixels are considered to be part of the same source. This comparison is done for each pixel in each level. To illustrate this process we present a schematic diagram in Fig. 5 that shows a complex emission profile that is divided in 23 sub-levels, at the 10th level the source is separated in two branches then at the 12th level the first branch is separated again in two sources A and B, at the level 17th there is a small separation at the branch B, but the ratio of the integrated intensity of this pseudo new branch is lower than the ratio defined to separate sources so it is declared as part of the B branch. The process continues until the last level at which point seven discrete sources have been identified.

#### 4. Artificial sources

In order to check the reliability of the compact source catalogue, we test our extraction algorithm on maps with artificial sources with known properties. To test the influence of the background emission in the extraction of sources, we created maps with uniform and varying background noise. These two cases allow us to compare the performance of the extraction algorithm in the

<sup>4</sup> CUPID is part of the STARLINK software suite (<http://starlink.jach.hawaii.edu>).

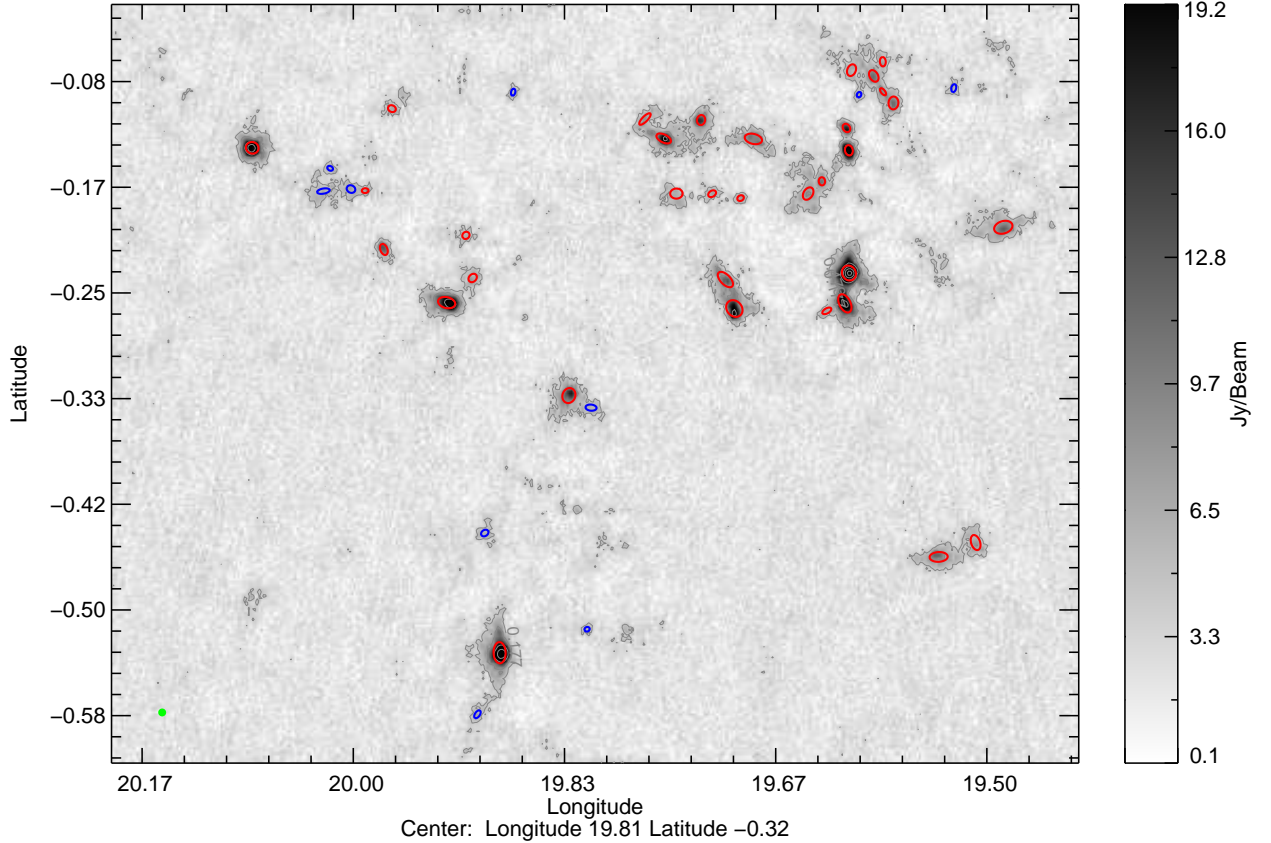


**Fig. 4.** Example of the sources extracted. The field shown in greyscale is the region outlined in red in the left panel of Fig. 3. The positions and sizes of sources identified by SExtractor are shown as red and blue ellipses. The red ellipses indicate to the most reliable detections, while the blue ellipses indicated the detections associated with higher flag values, given by SExtractor, which correspond to less reliable detections (see discussion in Sect. 5.1 for details). The ATLASGAL beam size is shown in green in the lower left corner of the map. Contours start at  $3\sigma$  (i.e.,  $0.18 \text{ Jy beam}^{-1}$ ) and increase with steps of 0.48, 1.61, 4.32, 8.96,  $15.89 \text{ Jy beam}^{-1}$ .

idealised case where the background is smooth and the more realistic case when the sources are intermixed with large scale diffuse emission.

The varying background noise map was created from the residual maps produced by SExtractor. The field used in this test is the map located at  $19.5^\circ$ , which is fairly representative of the rest of the ATLASGAL maps. The residual map contains background emission and zeros at the position of the extracted sources. The test map was smoothed using a boxcar function with a width of 10 pixels to remove the sharp ridges left by the source removal. These steps produced an emission map with varying noise properties similar to the emission seen in the ATLASGAL maps.

We used the CUPID task MAKECLUMPS to generate a catalogue of artificial objects with a uniform distribution in  $\ell$ ,  $b$ . The flux of the injected objects was uniformly distributed between 0.01 and  $0.75 \text{ Jy beam}^{-1}$ , however, the source size was set to a FWHM of 5 pixels ( $30''$ ) with a Gaussian shape. Taking these input parameters and using the test field as a template, MAKECLUMPS allowed us to produce a field of artificial sources with some added noise that has the same dimensions and coordinates of the test field. To produce the varying background test field we did not add additional noise with the algorithm but simply co-added the artificial

source map with the varying background noise map described in the previous paragraph. For the uniform background test field we simply used the output produced by the MAKECLUMPS task but this time set the noise level to be similar to the original map (i.e.,  $\sim 60 \text{ mJy beam}^{-1}$ ).

We repeated this process to produce 20 artificial source maps, all with both a varying and uniform background noise level. This group of 20 maps produced a catalogue of  $\sim 5000$  artificial sources, which is comparable to the number of genuine sources detected in the region presented here. For the varying background noise maps we produced background subtracted signal-to-noise maps following the same procedure used for the real ATLASGAL maps (see Sect. 3 for further details). SExtractor was then run on these artificial source maps using the same parameters as those used for the construction of the real catalogue. To compare the dependence of completeness on the background, the same extraction algorithm was tested on the maps with uniform noise. However, for these there was no need to try and filter the large scale variations in the background and therefore SExtractor was used directly on the simulated maps.

In Fig. 6 we plot the number of sources recovered as a function of input peak flux for the uniform and varying background noise maps (indicated by the blue and red lines, respectively).

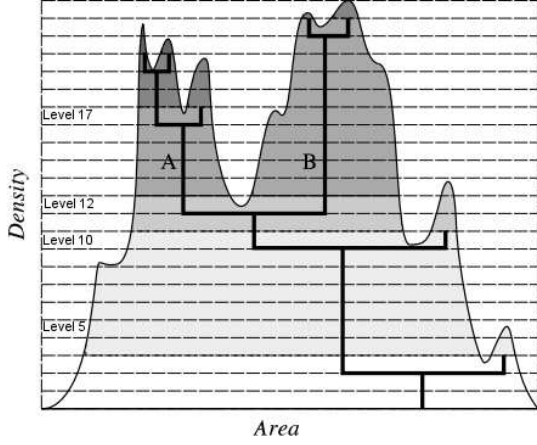


**Fig. 5.** Example of the deblending process. The dependence of a pixel to one source or another will depend on the relative integrated intensities (grey area) of their adjacent pixel for each level (dotted lines). This figure has been reproduced here with permission from Bertin & Arnouts (1996).

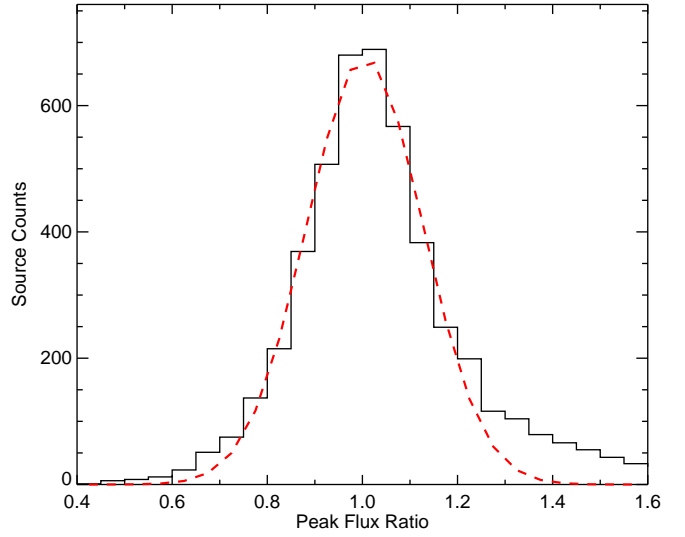
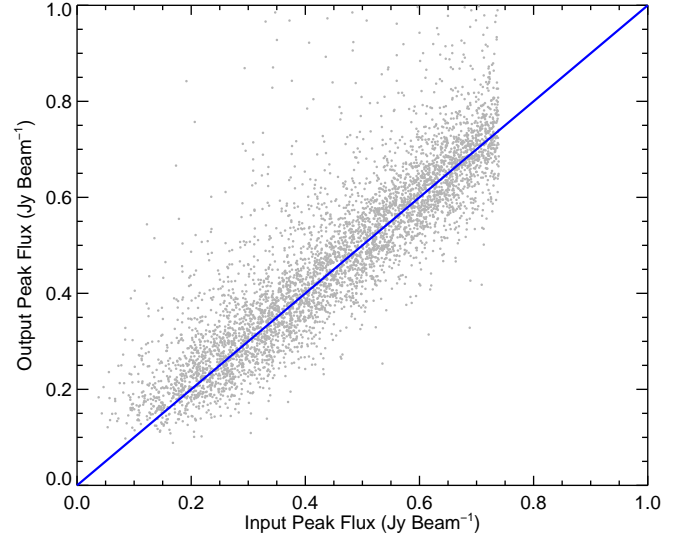


**Fig. 7.** In the upper panel we present a comparison of the recovered values for the peak fluxes values to the input values of the injected sources on the maps with varying background. The blue line represents equality. In the lower panel we present the recovered to injected flux ratio (black histogram) and the results of a Gaussian fit to values less than 1.2 (dashed red line).

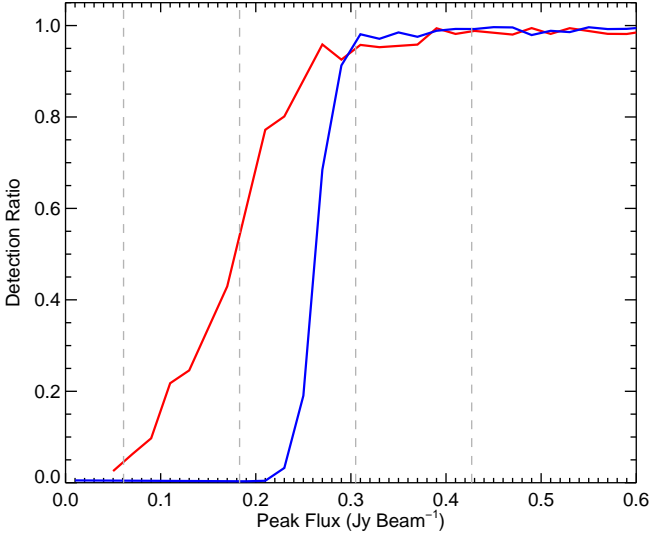


**Fig. 6.** Detection ratio of recovered to injected sources as a function of input peak fluxes. The blue solid and red dashed lines show the detection ratios for sources injected onto a uniform and varying background noise map, respectively. The dashed vertical lines indicate (from left to right) the  $1\sigma$ ,  $3\sigma$ ,  $5\sigma$ , and  $7\sigma$  noise levels.

In the case of the uniform noise level the source extraction algorithm is more than 99% complete above  $\sim 0.3 \text{ mJy beam}^{-1}$ , which corresponds to approximately  $5\sigma$ . The shape of the detection ratio and the  $5\sigma$  completeness level found for the uniform background noise maps is very similar to that found for the BGPS (Rosolowsky et al. 2010). However, the completeness profile determined from the sources injected and recovered from the varying background noise, which is much more realistic, is very different. In the case of the uniform background noise maps no sources are detected below the  $\sim 3\sigma$  level, however, we start to detect sources at  $\sim 1\sigma$  when adopting varying-background-noise maps. The detection of low peak flux sources is better in the varying background noise maps compared to those with uniform noise. This is because the peak fluxes are boosted by the

diffuse continuum emission they have been injected onto. As a consequence, the fluxes of weaker sources ( $<5\sigma$ ) are somewhat less reliable in this case.

We also note that for the varying background noise case the  $\sim 99\%$  completeness is obtained for peak fluxes above  $\sim 0.4 \text{ mJy beam}^{-1}$ , which, at approximately  $6\sigma$ , is slightly worse than that found for the uniform background noise case. This difference can be attributed to the presence of the diffuse low surface brightness emission which makes it more difficult to recover sources below  $<6\sigma$ . Clearly the presence of a varying background due to large scale diffuse emission has a significant impact on the detectability and reliability of fluxes for weaker sources (i.e.,  $<6\sigma$ ) and therefore we do not advise to use the sources below  $6\sigma$  blindly.

In the upper panel of Fig. 7 we compare peak flux of the recovered and injected sources. It is clear that these flux values are very well correlated and the injected and recovered fluxes are in

excellent agreement with each other (the blue line plotted over the data shows indicates equality). We also note the presence of a number of sources that have significantly higher recovered fluxes than input fluxes, which is a result of flux boosting from the varying background mentioned earlier. In the lower panel of Fig. 7 we present a histogram of the ratio of the injected and extracted flux values for each source. The distribution profile below a ratio value of 1.2 can be approximated by a Gaussian fit to the data (shown as a dashed red line on the plot) with a peak at  $\sim 1$  and has a  $\sigma$  of 0.12, which would suggests that the flux values extracted for the sources in this catalogue are generally well determined with an uncertainty of 12%, however, for a small number of sources in more complex regions the flux can be overestimated by up to a factor of 2.

## 5. Compact source catalogue

### 5.1. Catalogue description

SExtractor was run on each of the seventeen  $3^\circ \times 3^\circ$  fields that make up the inner most portion of the ATLASGAL survey (i.e.,  $330^\circ < \ell < 21^\circ$ ). The results obtained for each field were subsequently combined in order to compile a complete catalogue of sources, taking care to eliminate duplicated sources located in the overlap regions between adjoining fields. In total we have identified 6639 sources in the  $153 \text{ deg}^2$ .

In Table 1 we present a sample of the catalogue (for the region presented in Fig. 4) as an example of its form and content. The full and up-to-date catalogue and ATLASGAL emission maps will be hosted by the ATLASGAL project page<sup>5</sup>, the ESO<sup>6</sup> and CDS<sup>7</sup> database. There will be incremental improvements in image processing, calibration and source extraction. In the table we present the source name, the source peak and barycentric position, the size of the semi-major and minor axis and their position angle, the deconvolved radius, the peak and integrated fluxes and their associated errors and any warning flags generated by the algorithm (see full bit per bit description below).

The source names are based on the Galactic coordinates of the peak flux position, which are given in Cols. 2 and 3. The barycentric coordinates are determined from the first order moments of the longitude and latitude profiles. The barycentric position generally defines the centre position of a source, however, if the emission profile of a source is strongly skewed or is associated with substructures, the peak position can be a more accurate measure of a source's position. The source sizes describe the detected source as an elliptical shape, although no fitting is actually performed. The semi-major and semi-minor axis lengths represent the standard deviation of the pixel co-ordinate values about the centroid position, weighted by the pixel values. The position angle is given as anti-clockwise from Galactic north.

Since the source sizes are determined only using the pixels above the detection threshold it is likely these underestimate the true source sizes, and in some cases results in source sizes that are smaller than the beam. Following Rosolowsky et al. (2010) we estimate the angular radius ( $\theta_R$ ) from the geometric mean of the deconvolved major and minor axes and multiplied by a factor  $\eta$  that relates the r.m.s. size of the emission distribution of the source to its angular radius (Eqn. 6 of Rosolowsky et al. 2010):

$$\theta_R = \eta \left[ (\sigma_{\text{maj}}^2 - \sigma_{\text{bm}}^2)(\sigma_{\text{min}}^2 - \sigma_{\text{bm}}^2) \right]^{1/4}, \quad (1)$$

where  $\sigma_{\text{bm}}$  is the r.m.s. size of the beam (i.e.,  $\sigma_{\text{bm}} = \theta_{\text{FWHM}} / \sqrt{8 \ln 2} \simeq 8''$ ). The value of  $\eta$  depends on the size of the source with respect to the beam and the emission distribution. Rosolowsky et al. (2010) adopted a value of 2.4, which is the median of the values derived from a range of models, however, they note that the value of  $\eta$  can vary by a factor of 2 in their simulations. For consistency and to facilitate comparisons between the BGPS and ATLASGAL catalogues we also adopt this value, which is approximately equivalent to the sources effective radius (i.e.,  $R_{\text{eff}} = \sqrt{A/\pi}$ , where  $A$  is the surface area of the source; Dunham et al. 2011).

The peak flux is directly obtained from SExtractor, however, since the algorithm treats each pixel in the given emission map in a statistically independent manner and the ATLASGAL maps are gridded with  $\sim 3$  pixels per beam it is necessary to account for the beam area to determine the final measured fluxes and their associated uncertainties. This was simply done by dividing the derived flux values by the beam area (i.e.,  $1.133 \times \text{FWHM}^2 \simeq 11.6$  pixels). The errors given for the peak and integrated fluxes include the absolute calibration uncertainty of 15% mentioned in Sect. 2 (see also Schuller et al., 2009 for details) combined in quadrature with the intrinsic measurement error. In the case of the integrated flux this is provided by SExtractor, however, the error in the peak flux is derived from the local r.m.s. noise in the image.

In Col. 15 we present the quality flag given by SExtractor which gathers all the information about possible problems or artefacts affecting the source (Bertin & Arnouts, 1996). For each source, this flag is either zero (no particular problem), or is equal to the sum of one or more number(s) with the following meanings: (1) the object has neighbours, bright and close enough to significantly bias the photometry, or bad pixels (more than 10% of the integrated area affected); (2) the object was originally blended with another one; (4) at least one pixel of the object is saturated (or very close to); (8) the object is truncated (too close to an image boundary); (16) object's aperture data are incomplete or corrupted; (32) object's isophotal data are incomplete or corrupted; (64) a memory overflow occurred during deblending; (128) a memory overflow occurred during extraction. For example, a flag value of 10 means that the object was originally blended with another source *and* that it is truncated because is located too close to the edge of the map. In the final column of the table we present the signal to noise for each source.

In Fig. 4 we overplot the positions of sources detected by SExtractor towards a small region to demonstrate its performance. To check the reliability of sources with high flag values we plot sources with flag values less than 4 (which are the most reliable) in red while those with higher flag values are shown in blue. In this example region it is clear that the sources with the higher flag values are associated with genuine emission, however, the emission does appear to be weaker and more diffuse than found to be associated with the lower flag value detections. A similar situation is seen in other regions examined and so we conclude that these high flag detections do identify genuine sources of emission, but with the caveat that their associated parameters are somewhat less reliable.

### 5.2. Catalogue properties

In this section we will look at the Galactic distribution of sources detected and the overall distribution of their derived parameters. As a check on the reliability of the ATLASGAL catalogue we compare our results to those obtained from the Bolocam Galactic

<sup>5</sup> [www.mpi-fr-bonn.mpg.de/div/atlasgal/](http://www.mpi-fr-bonn.mpg.de/div/atlasgal/)

<sup>6</sup> Available through <http://archive.eso.org/wdb/wdb/adp/phases>

<sup>7</sup> <http://cdsweb.u-strasbg.fr/cgi-bin/qcat?J/A+A/>

**Table 1.** The ATLASGAL compact source catalogue. The columns are as follows: (1) name derived from Galactic coordinates of the maximum intensity in the source; (2)-(3) Galactic coordinates of maximum intensity in the catalogue source; (4)-(5) Galactic coordinates of emission centroid; (6)-(8) semi-major and semi-minor size and source position angle measured anti-clockwise from Galactic north; (9) effective radius of source; (10)-(13) peak and integrated flux densities and their associated uncertainties; (14) SExtractor detection flag (see text for details); (15) signal to noise ratio (SNR) — values for sources with peak flux below  $6\sigma$  detection should not be used blindly.

Name	$\ell_{\max}$	$b_{\max}$	$\ell$	$b$	$\sigma_{\text{maj}}$	$\sigma_{\text{min}}$	PA	$\theta_{\text{R}}$	$S_{\text{peak}}$	$\Delta S_{\text{peak}}$	$S_{\text{int}}$	$\Delta S_{\text{int}}$	Flag	SNR
(1)	( $^{\circ}$ )	( $^{\circ}$ )	( $^{\circ}$ )	( $^{\circ}$ )	( $''$ )	( $''$ )	( $^{\circ}$ )	( $''$ )	( $\text{Jy beam}^{-1}$ )		( $\text{Jy}$ )		(14)	(15)
AGAL019.486–00.199	19.486	−0.199	19.487	−0.198	27	17	73	48	0.80	0.13	9.35	1.67	2	12.9
AGAL019.508–00.447	19.508	−0.447	19.509	−0.447	22	13	161	34	0.48	0.10	4.06	0.86	0	7.6
AGAL019.526–00.086	19.526	−0.086	19.526	−0.089	11	7	14	...	0.35	0.08	1.59	0.45	0	5.6
AGAL019.539–00.456	19.539	−0.456	19.538	−0.458	26	14	87	40	0.76	0.13	7.72	1.42	2	11.2
AGAL019.572–00.101	19.572	−0.101	19.574	−0.100	18	14	4	33	0.71	0.13	4.13	0.87	2	8.7
AGAL019.581–00.069	19.581	−0.069	19.582	−0.068	13	8	176	11	0.48	0.10	3.90	0.83	3	6.5
AGAL019.582–00.091	19.582	−0.091	19.582	−0.091	12	6	142	...	0.59	0.13	1.81	0.49	3	6.5
AGAL019.589–00.079	19.589	−0.079	19.589	−0.079	18	12	150	28	0.73	0.14	9.27	1.66	3	8.3
AGAL019.601–00.092	19.601	−0.092	19.601	−0.094	8	6	24	...	0.40	0.11	1.49	0.43	0	4.2
AGAL019.606–00.072	19.606	−0.072	19.607	−0.074	17	12	22	28	0.46	0.11	6.35	1.22	3	5.6
AGAL019.609–00.137	19.609	−0.137	19.609	−0.138	15	11	169	23	2.79	0.43	7.59	1.40	3	32.3
AGAL019.609–00.234	19.609	−0.234	19.609	−0.234	22	19	151	45	19.20	2.88	44.85	7.01	3	252.3
AGAL019.611–00.121	19.611	−0.121	19.611	−0.120	13	10	147	18	1.17	0.20	2.86	0.66	3	13.8
AGAL019.612–00.259	19.612	−0.259	19.612	−0.258	28	16	153	46	1.88	0.29	14.88	2.51	3	25.7
AGAL019.628–00.264	19.628	−0.264	19.626	−0.264	14	7	60	...	0.46	0.10	1.62	0.45	3	6.8
AGAL019.631–00.162	19.631	−0.162	19.630	−0.162	12	9	175	13	0.70	0.14	5.80	1.13	3	7.9
AGAL019.641–00.172	19.641	−0.172	19.641	−0.172	19	13	32	32	0.53	0.12	11.06	1.93	2	5.7
AGAL019.686–00.127	19.686	−0.127	19.684	−0.129	25	14	103	40	0.70	0.14	7.52	1.39	2	8.2
AGAL019.694–00.174	19.694	−0.174	19.694	−0.175	10	8	62	...	0.44	0.10	1.02	0.34	0	6.0
AGAL019.699–00.266	19.699	−0.266	19.699	−0.262	26	21	138	52	1.97	0.30	12.69	2.18	3	27.7
AGAL019.706–00.239	19.706	−0.239	19.706	−0.239	27	14	136	41	0.88	0.15	9.56	1.71	3	12.1
AGAL019.716–00.171	19.716	−0.171	19.717	−0.172	12	8	58	10	0.44	0.10	2.62	0.63	0	5.7
AGAL019.726–00.114	19.726	−0.114	19.726	−0.114	14	11	10	23	1.09	0.18	7.61	1.41	0	12.5
AGAL019.746–00.171	19.746	−0.171	19.745	−0.172	18	14	88	33	0.40	0.09	3.93	0.84	2	6.0
AGAL019.754–00.129	19.754	−0.129	19.755	−0.128	22	11	116	30	1.87	0.29	11.23	1.96	2	20.9
AGAL019.771–00.114	19.771	−0.114	19.770	−0.113	22	7	45	...	0.54	0.10	2.78	0.65	2	8.3
AGAL019.811–00.342	19.811	−0.342	19.812	−0.340	16	9	95	15	0.37	0.08	3.27	0.73	19	6.0
AGAL019.817–00.516	19.817	−0.516	19.816	−0.515	8	6	68	...	0.33	0.08	1.20	0.38	0	5.3
AGAL019.829–00.329	19.829	−0.329	19.830	−0.331	22	18	20	43	1.15	0.19	9.90	1.76	2	17.2
AGAL019.874–00.092	19.874	−0.092	19.874	−0.092	10	6	13	...	0.32	0.08	1.08	0.36	0	5.3
AGAL019.882–00.534	19.882	−0.534	19.885	−0.534	30	17	178	50	7.43	1.12	27.37	4.39	2	90.7
AGAL019.899–00.441	19.899	−0.441	19.896	−0.439	11	9	56	10	0.35	0.08	2.51	0.61	18	5.7
AGAL019.902–00.582	19.902	−0.582	19.902	−0.582	13	7	35	...	0.38	0.09	3.24	0.73	16	5.9
AGAL019.906–00.241	19.906	−0.241	19.906	−0.238	13	10	44	20	0.45	0.10	3.33	0.74	0	5.8
AGAL019.911–00.206	19.911	−0.206	19.911	−0.205	11	10	45	15	0.33	0.08	2.30	0.57	0	4.9
AGAL019.922–00.259	19.922	−0.259	19.926	−0.258	25	15	103	42	2.51	0.38	13.96	2.37	0	36.8
AGAL019.967–00.106	19.967	−0.106	19.970	−0.105	11	9	116	14	0.45	0.09	2.29	0.57	0	7.2
AGAL019.977–00.214	19.977	−0.214	19.976	−0.216	16	10	158	21	0.87	0.15	3.12	0.70	0	13.9
AGAL019.991–00.169	19.991	−0.169	19.991	−0.169	10	7	86	...	0.55	0.11	1.52	0.43	3	7.9
AGAL020.004–00.167	20.004	−0.167	20.002	−0.168	13	10	115	19	0.40	0.09	4.63	0.95	18	5.7
AGAL020.019–00.151	20.019	−0.151	20.018	−0.152	9	6	119	...	0.37	0.09	1.96	0.51	16	5.0
AGAL020.022–00.169	20.022	−0.169	20.024	−0.170	18	7	80	...	0.38	0.09	5.80	1.13	19	5.5
AGAL020.081–00.136	20.081	−0.136	20.080	−0.136	18	16	106	36	7.68	1.15	18.43	3.04	0	119.8

Notes: Only a small portion of the data is provided here, the full table is only available in electronic form at the CDS via anonymous ftp to [cdsarc.u-strasbg.fr](mailto:cdsarc.u-strasbg.fr) (130.79.125.5) or via <http://cdsweb.u-strasbg.fr/cgi-bin/qcat?J/A+A/>.

Plane Survey (BGPS; Aguirre et al. 2011) that were recently presented by Rosolowsky et al. (2010).

The BGPS covers  $150 \text{ deg}^2$  of the Galactic plane, including the majority of the first quadrant with a latitude range of  $|b| < 0.5^{\circ}$ . Although the overlap between the BGPS and the ATLASGAL region presented in this paper is relatively modest ( $\sim 30 \text{ deg}^2$ ) when compared to the total area covered by the two surveys, the overlapping region does contain some of the highest density regions in the plane, and thus, provides a large number of sources in common to both surveys. Another thing to

bear in mind when comparing the two catalogues is that the two surveys were performed at different wavelengths and hence they have different spatial resolution and sensitivity and so we do not expect a one to one correlation between individual sources or their parameters. However, we do expect the overall distribution of source parameters to be correlated. To facilitate the comparisons between the two catalogues we have followed the structure and present the same parameters in Table 1 as are given in the BGPS catalogue (cf. Table 1; Rosolowsky et al. 2010).

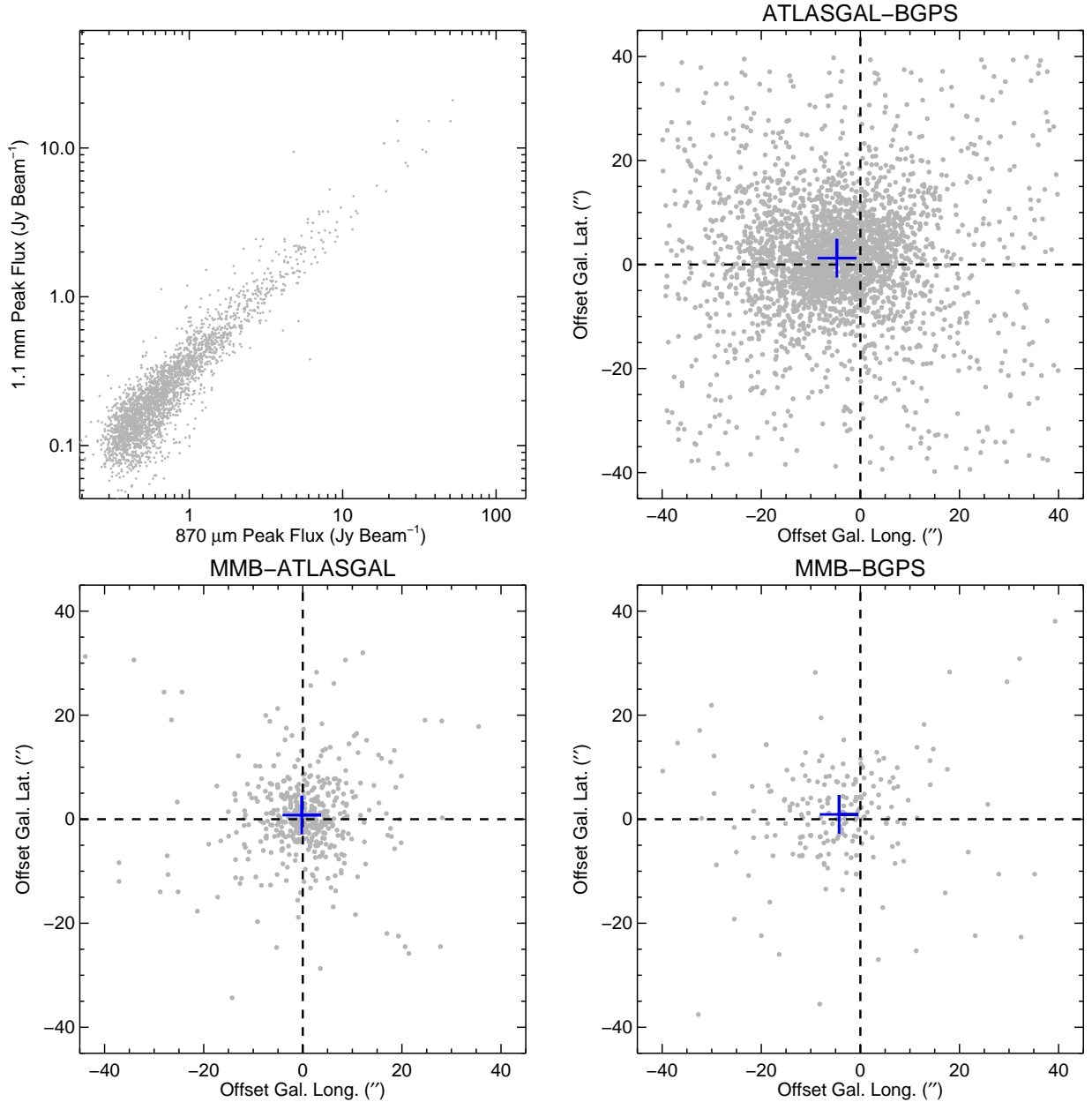


**Fig. 8.** Results of the cross-matching performed between the ATLASGAL, BGPS and MMB catalogues. In the upper left panel we plot the peak fluxes for BGPS and ATLASGAL sources found within a matching radius of  $40''$ . In the upper right panel we compare the angular offsets in Galactic longitude and latitude between the ATLASGAL and BGPS catalogues. In the two lower panels we present plots showing the angular offsets in  $\ell$  and  $b$  between matched MMB-ATLASGAL (left) and MMB-BGPS (right) sources. The dashed lines overplotted in the in the upper right and lower panels show the zero offset positions in  $\ell$  and  $b$ , while the blue crosses indicate the mean offset of the matched samples.

### 5.2.1. Astrometry

In order to check the astrometry of the ATLASGAL catalogue we compared the peak positions determined in our catalogue with those determined by the BGPS. Using an angular search radius of  $40''$  we identify  $\sim 3,000$  likely associations. The matching radius was chosen to be a little larger than the resolution of the BGPS to obtain a large sample of matched sources to compare the positions, while it is still small enough to avoid multiple matches between sources. In the upper left panel of Fig. 8 we plot the peak  $870\mu\text{m}$  and  $1.1\text{ mm}$  flux densities of the associated sources. As this plot shows, there is a strong correlation

between the fluxes of the matched sources which suggests that the matched sources are really associated with each other.

In the upper right panel of Fig. 8 we plot the angular position offsets in Galactic Longitude and Latitude between the matched ATLASGAL and BGPS sources. Although we should expect a spread in the angular offsets for individual matched pairs of sources, given the large number of matches we also expect the mean of the offset distribution to be centred around zero. However, visual inspection of this plot reveals a systematic offset between the two catalogues of  $\sim 5''$  in latitude (see Table 2 for details). This offset is comparable to the pixel sizes for the two surveys ( $6''$  and  $7''$  for ATLASGAL and BGPS, respectively).

**Table 2.** Angular offsets between peak flux positions determined from the ATLASGAL, BGPS and MMB catalogues. The errors given are the standard errors.

Catalogues	$\Delta\ell$	$\Delta b$	Matches
ATLASGAL-BGPS	$-4.74 \pm 0.26$	$+1.23 \pm 0.23$	2803
MMB-ATLASGAL	$-0.20 \pm 0.51$	$+0.79 \pm 0.43$	459
MMB-BGPS	$-4.30 \pm 0.86$	$+0.92 \pm 0.70$	209
SCUBA-BGPS <sup>a</sup>	$-1.8 \pm 1.2$	$+0.4 \pm 0.8$	...

<sup>a</sup> These results have been taken from Aguirre et al. (2011).

Given that this offset is significantly smaller than their respective beam size, and that the BGPS and ATLASGAL sources are not point sources, means that this systematic offset cannot be seen from a comparison of contoured emission maps of individual sources. However, the offset is approximately 20 times the standard error and is therefore significant.

In an effort to track down the origin of this offset we repeated the matching procedure described at the beginning of this subsection with the Methanol Multibeam (MMB) survey catalogue (Green et al. 2009). The MMB catalogue consists of  $\sim 700$  methanol masers observed at high resolution with the Australia Telescope Compact Array which has provided positions accurate to better than an arcsecond r.m.s. (Caswell et al. 2010). Methanol masers are associated with the early stages of high-mass star formation, which takes place within deeply embedded dust clumps. We should therefore expect a strong positional correlation between the methanol masers and dust clumps identified by ATLASGAL. We have matched  $\sim 500$  masers with ATLASGAL sources and present a plot of their positional offsets in the lower left panel of Fig. 8. It is clear from this plot and from the mean offsets and standard errors presented in Table 2 that there is no significant offset between the two catalogues.

We also computed the positional offsets between the BGPS and MMB catalogues (see lower right panel of Fig. 8). We find a very similar systematic offset ( $\Delta\ell \approx 5''$ ) as found from the comparison of the ATLASGAL and BGPS catalogues shown in the upper right panel of Fig. 8. Although the number of matches found between the MMB and BGPS samples is smaller ( $\sim 200$ ) the mean offset in longitude is five times the standard error and is therefore significant.

Aguirre et al. (2011) checked the astrometry of the BGPS catalogue against the SCUBA Legacy Catalogue (Di Francesco 2008; hereafter SLC) and found the offsets between them to be  $\Delta\ell = -1.8'' \pm 1.2''$  and  $\Delta b = 0.4'' \pm 0.8''$ .<sup>8</sup> The mean offset values and their associated error reported by Aguirre et al. (2011) are consistent with the zero offset position in longitude and latitude. However, because their standard errors are quite large their results are consistent with the values determined here for the offset between the ATLASGAL and BGPS sources (i.e., within 3 standard errors). The excellent angular correlation between the MMB and ATLASGAL sources, and the fact that the same systematic offset is observed when comparing the ATLASGAL and MMB catalogues with the BGPS, would suggest that the observed systematic offset originates from the BGPS catalogue.

<sup>8</sup> In the Aguirre et al. (2011) paper they give the offsets determined from the difference between the BGPS and SCUBA fields, however, to be consistent with the way the offsets have been determined here these values have been reversed.

## 5.2.2. Galactic distribution

In Fig. 9 we present histograms showing the Galactic longitude and latitude distribution of the ATLASGAL catalogue (left and right panels, respectively). Inspection of the longitude distribution reveals a number of peaks in the source counts; these are located at approximately  $-27^\circ$ ,  $-22^\circ$ ,  $-8^\circ$ ,  $0^\circ$  with a weaker peak at  $14^\circ$ . The Galactic structure traced by ATLASGAL sources was the subject of a recent paper by Beuther et al. (2012). The authors used the CLUMPFIND source extraction algorithm to produce a source catalogue and they analysed the distribution in Galactic longitude. They found that the positions of the peaks in source counts coincide with the positions of the tangent of spiral arms and individual star forming regions. Identifying the peaks in the source counts with the tangent of the Norma arm ( $-28^\circ$ ), the farside of the Near 3-kpc arm ( $-22^\circ$ ), the NGC6334/NGC6357 star forming regions ( $-8^\circ$ ), the Galactic centre region and finally M16 and M17 regions ( $+15^\circ$ ), respectively.

Comparing the longitude distribution of ATLASGAL sources with the BGPS distribution we see that they are similar, both showing the same peaks, however, we note that the ratio of the Galactic centre peak to the other peaks is quite different. This is likely due to the different spatial resolution of the two surveys. The complex emission seen towards the Galactic centre is more easily deblended in the ATLASGAL data due to the higher spatial resolution which results in a higher number of sources detected in this region. Conversely, the lower resolution BGPS survey is more sensitive to lower surface brightness structures resulting in a higher proportion of sources being found away from the Galactic centre.

The latitude distribution shown in the right panel of Fig. 9 peaks significantly below  $0^\circ$  as also noted by Schuller et al. (2009) and more recently by Beuther et al. (2012). This offset is consistent with the location of the Sun above the Galactic plane (Humphreys & Larsen, 1995). Comparing the latitude distribution to that of the BGPS we find them again to be similar. Both ATLASGAL and BGPS distributions have the same FWHM. We note that the tails of the distributions appear to be significantly different, however, the BGPS latitude range is  $|b| < 0.5^\circ$  with only a few excursions to larger value of  $|b|$  and so the distributions are not really comparable for latitudes  $|b| > 0.5^\circ$ .

## 5.2.3. Flux distribution

In Fig. 10 we show the peak and integrated flux distributions for the ATLASGAL sources (grey filled histogram) and the BGPS sources located in the overlap region (blue histogram). These distributions show the differential flux density spectrum (i.e.,  $dN/dS \nu \approx \Delta N/\Delta S \nu \propto S^{-\alpha}$ ; Rosolowsky et al. 2010). Comparing the distributions of the peak and integrated fluxes for the two catalogues they seem to be very similar, however, with the higher frequency measurements being shifted to higher values.

The flux distributions above the turnover can be approximated by a power-law that extends over three orders of magnitude. Fitting these parts of the distributions with a linear least-squares fit we find that the peak and integrated distributions can be represented by the values of  $\alpha = 2.4 \pm 0.04$  and  $2.3 \pm 0.06$ , respectively. The results of these fits are indicated by the red lines overplotted on the left and right panels of Fig. 10. The values obtained from the same fit to the BGPS peak and integrated flux distributions are 2.4 and 1.9, respectively (Rosolowsky et al. 2010). We note that the fit to the integrated fluxes is significantly steeper for the ATLASGAL catalogue than determined for the

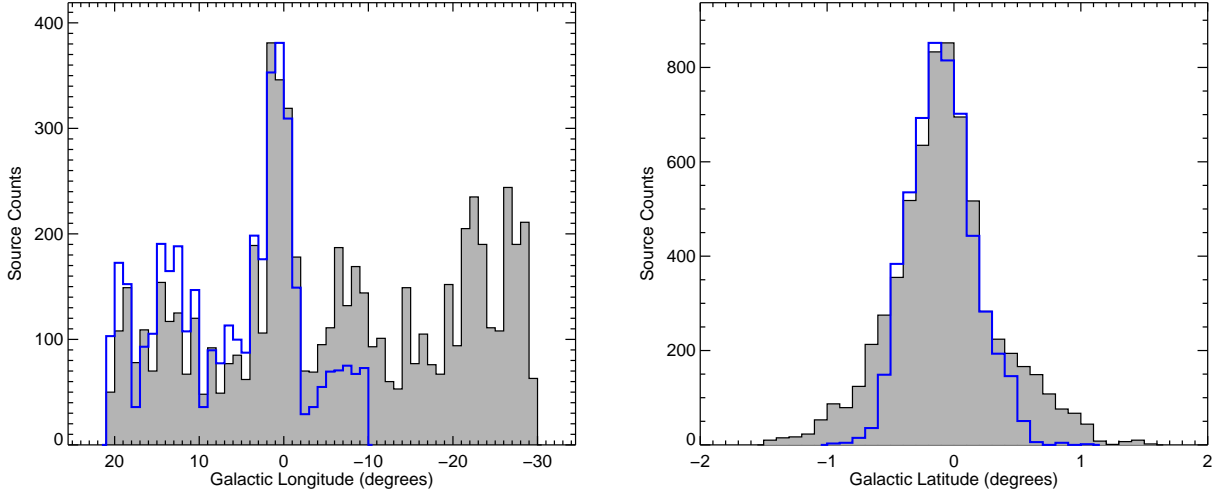


**Fig. 9.** Histograms of the Galactic longitude and latitude distribution for ATLASGAL sources extracted by SExtractor (grey filled histogram) and the BGPS (blue histogram). In both plots the peak of the BGPS distribution has been normalised to the peak of the ATLASGAL distribution. The bin sizes used for the longitude (left panel) and latitude (right panel) distributions is  $1^\circ$  and  $0.1^\circ$ , respectively.

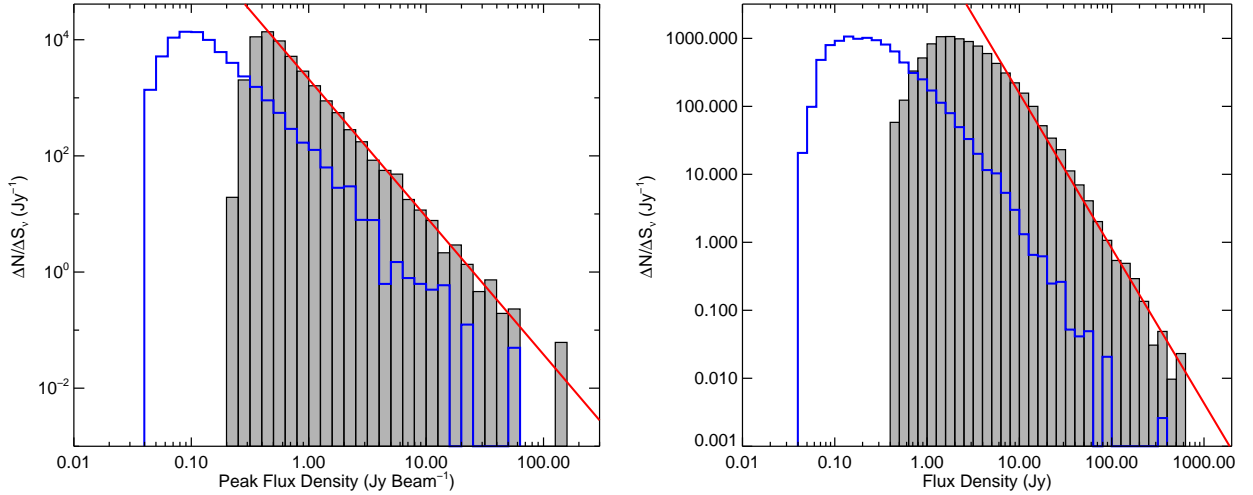


**Fig. 10.** Flux density number distribution for ATLASGAL sources extracted by SExtractor (grey filled histogram) and the BGPS (blue histogram). In both plots the peak of the BGPS distribution has been normalised to the peak of the ATLASGAL distribution. In the left and right panels we present histograms of the peak and integrated flux densities measured for each source respectively. The red line on each plot shows the result of a linear least-squares fit to flux densities larger than the peak of each distribution.

BGPS catalogue. This probably results from the different resolutions between with two surveys as the lower resolution BGPS survey is likely to blend smaller clumps, that are resolved in ATLASGAL, together into larger clumps with higher integrated fluxes. This leads to a higher proportion of the BGPS sources being found at higher fluxes and the shallower slope than found for the ATLASGAL catalogue.

The difference in the slope between the peak and integrated flux densities results from the fact that point sources dominate the peak distribution towards the completeness limit, whereas brighter sources tend to be larger and thus have larger total flux densities than for the smaller sources. As pointed out by Rosolowsky et al. (2010), this makes the integrated flux density

distribution top-heavy and effectively lowers the magnitude of the exponent.

Another interesting feature of the peak distribution is that the main body of the distribution drops off completely at  $\sim 70 \text{ Jy beam}^{-1}$ , however, there is another outlying peak located at  $\sim 150 \text{ Jy beam}^{-1}$ . The bright sources that contribute to this flux density bin are the brightest  $870 \mu\text{m}$  sources in the catalogue and form part of a dust ridge associated with the Sgr B2 high-mass star forming region.

#### 5.2.4. Angular size distribution

In Fig. 11 we present plots showing the size distributions of the catalogued sources. In the upper panel of this figure we show

histograms of the semi-major ( $\sigma_{\text{maj}}$ ) and semi-minor ( $\sigma_{\text{min}}$ ) distributions and the ATLASGAL beam size ( $\sigma_{\text{bm}} \simeq 8''$ , red dotted line). We note that there is a significant number of sources with sizes smaller than the beam, particularly with regard to the semi-minor axis. This is due to the fact that the sizes are derived from moment measurements of the emission distribution above the threshold value ( $\sim 3\sigma_{\text{r.m.s.}}$ ) and therefore do not take account of all of the emission associated with each source down to the zero-intensity level. As previously noted by Rosolowsky et al. (2010) this has a disproportionate effect on weaker sources and often results in their sizes being underestimated. We find the mean and median values of the peak fluxes for sources in our catalogue that are smaller than the beam are  $0.52$  and  $0.43 \text{ Jy beam}^{-1}$ , respectively, and therefore this sample is dominated by sources around the sensitivity limit with only a few percent having peak fluxes above  $1 \text{ Jy beam}^{-1}$ .

In the middle panel of Fig. 11 we present a histogram showing the elongation distribution, that is the ratio of semi-major to semi-minor axes. The distribution has a peak and median value of  $1.3$  and  $1.6$ , respectively, which indicates that most sources in the catalogue are significantly elongated. The elongation distribution closely matches that found for the BGPS sources. The only noticeable difference is that the ATLASGAL catalogue tends to have a slightly higher degree of elongation, possibly a result of the higher resolution of ATLASGAL survey. However, both catalogues appear to contain a significant number of very elongated sources reflecting the fundamentally filamentary structure of molecular clouds.

In the lower panel of Fig 11 we present the effective radii of the ATLASGAL and BGPS detections. The two distributions again appear to be broadly similar, however, the whole BGPS source distribution appears to have been shifted  $10\text{--}15''$  to the right of the ATLASGAL distribution, which is clearly a result of the different survey resolutions.

## 6. Comparison with other Galactic plane surveys

### 6.1. Infrared catalogues

We performed a cross correlation of our catalogue with the far-infrared *IRAS* Point Source Catalogue (Joint Iras Science 1994), and with the mid-infrared Midcourse Space eXperiment (*MSX*) Point Source Catalogue (Egan et al. 2003). We used a search radius of  $30''$  around the peak flux position for all these survey catalogues. The resolution of the *MSX* survey and the APEX telescope used for ATLASGAL are very similar ( $18''$  and  $19.2''$ , respectively) making the correlation between both data sets relatively straightforward. This represents an initial attempt to associate ATLASGAL sources with their IR counterpart, and further associations with other catalogues (e.g. those extracted from the *Spitzer* GLIMPSE and MIPS GAL surveys) will be addressed in a future paper.

Infrared emission detected by the *IRAS* and *MSX* surveys generally implies that star formation is already underway within a clump, therefore, these surveys trace objects in a relatively evolved stage of star formation. The ATLASGAL catalogue presented here contains 6639 sources, of which we found 755 associated with *IRAS* sources and 2314 associated with *MSX* point sources. The number of sources with *IRAS* and *MSX* association is 645.

We found that 4216 objects, corresponding to 62% of the ATLASGAL sources, are not associated with any mid- or far-infrared point sources found in the *MSX* or *IRAS* catalogues. These objects are excellent candidates for cold dense clumps in

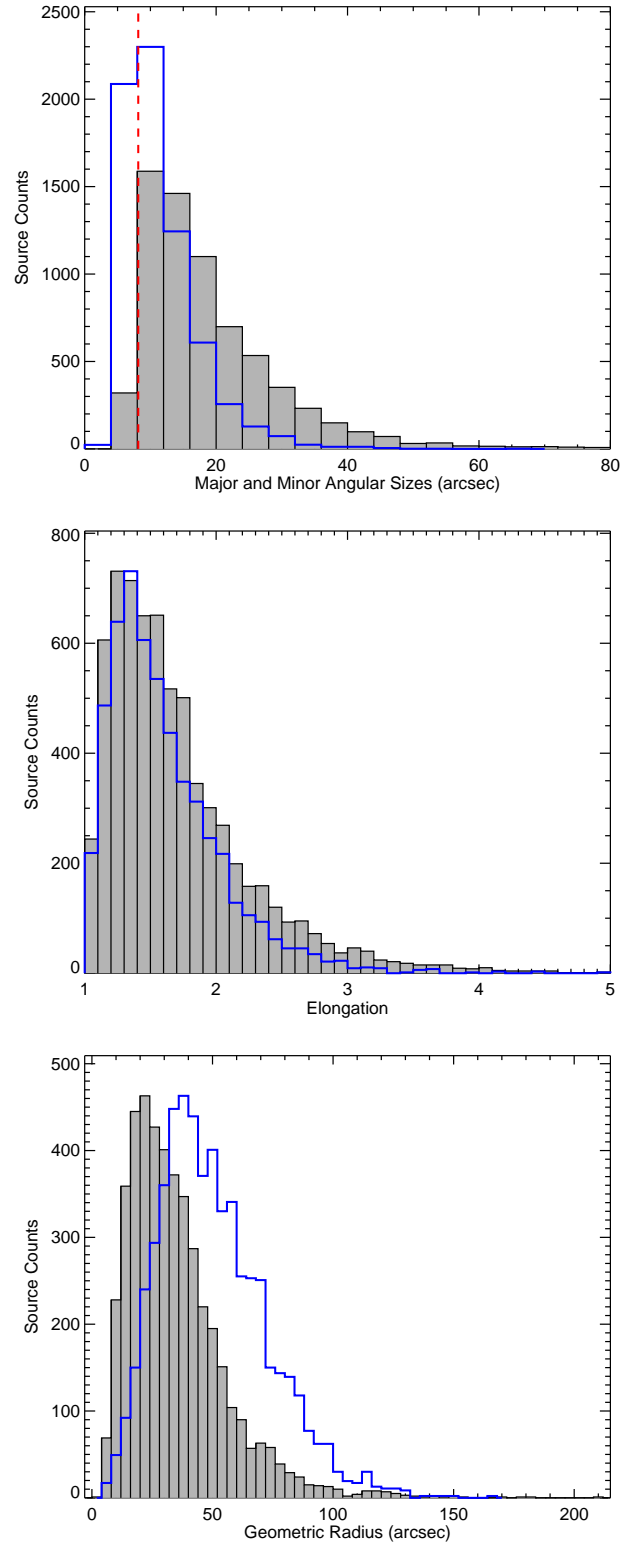


**Fig. 11.** Histograms of the angular size distribution of detected ATLASGAL sources. In the upper panel we show the distribution of the semi-major (filled grey histogram) and semi-minor (blue open histogram) size distributions of detected ATLASGAL sources. The red dashed line shows the ATLASGAL r.m.s. beam size. The bin size used for both parameters is  $4''$ . In the middle and lower panels we present histograms of the elongation and effective radii of ATLASGAL sources (grey filled histogram) and the BGPS (blue histogram). In both cases the peak of the BGPS distribution has been normalised to the peak of the ATLASGAL distribution. The bin sizes used for the elongation and radii distributions are  $0.1$  and  $4''$  respectively.

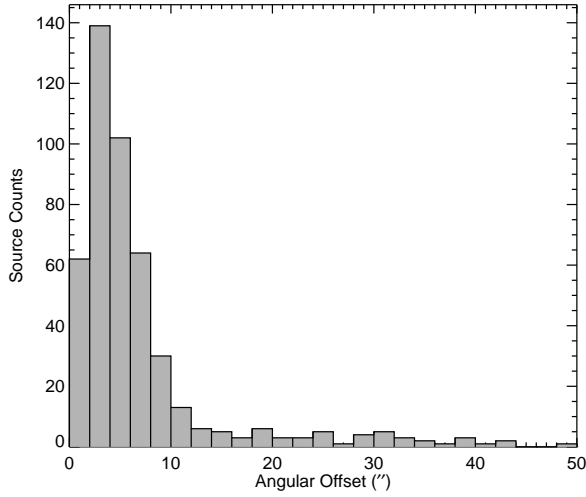


**Fig. 12.** Distribution of separation between methanol maser sources from the MMB survey and ATLASGAL sources. This plot has been truncated at an angular offset of  $50''$ , however, only 7 ATLASGAL-MMB associations have larger offsets than this. The bin size is  $2''$ .

an early stage of evolution, prior to the birth of high-mass protostars. Further correlation of these sources with other infrared surveys such as GLIMPSE or MIPS GAL, can give further information on their evolutionary stage, based on the presence or absence of star formation indicators such as green fuzzies (enhancement at  $4.5 \mu\text{m}$ , often referred to as extended green objects, e.g., Cyganowski et al. 2008) or  $24 \mu\text{m}$  point sources. Moreover, follow up studies of these cold dense clumps in molecular lines and their detailed study with next generation telescopes such as the ALMA and the Jansky VLA will help improve our understanding the initial stages of high-mass star formation.

## 6.2. Methanol masers

Methanol masers are well-known probes of early phases of high-mass star formation, in particular the strong  $6.7 \text{ GHz}$  Class-II maser (Menten, 1991). Recently a Galactic plane survey of this maser transition using a 7-beam receiver on the Parkes telescope has been completed (Green et al., 2009). These maser detections were followed up at high angular-resolution with the Australian Telescope Compact Array to obtain sub-arcsecond positional accuracy. To date the MMB has reported the positions of 707 methanol masers located between  $186^\circ < \ell < 20^\circ$  and  $|b| < 2^\circ$  (Caswell et al. 2010; Green et al. 2010; Caswell et al. 2011; Green et al. 2012), of these 493 are located within ATLASGAL fields presented in this paper (i.e.,  $330^\circ < \ell < 21^\circ$ ). Cross-matching these MMB sources with the ATLASGAL catalogue generated from the SExtractor algorithm we find 471 positional associations, which corresponds to  $\sim 96\%$  of the available MMB sources but only  $\sim 7\%$  of the ATLASGAL catalogue.

In Fig. 12 we show the angular separation between the ATLASGAL-MMB associations. The sharp peak seen towards small angular offsets reveals a strong correlation between the position of the methanol maser and the peak column density of each clump as traced by the submm continuum emission. We find that  $\sim 87\%$  of all ATLASGAL-MMB associations are found with angular separations  $< 12''$ , after which the distribution of the offsets flattens to an almost constant background level. We find that 61 ATLASGAL-MMB associations have angular off-

sets larger than  $12''$ ; this could indicate the presence of clumpy substructure that is smaller than the size of the APEX beam or a chance alignment with an MMB source associated with an undetected dust clump.

Inspection of the ATLASGAL maps at the locations of the 22 MMB sources not found to be associated with an ATLASGAL source reveals that nearly all of these masers are associated with either weak diffuse emission, which would have been filtered out by the background subtraction, or weak compact emission with sizes smaller than that of the APEX beam. Since methanol masers are almost exclusively associated with high-mass star forming regions it is very likely that the majority of these masers are located at the far side of the Galaxy. These masers have peak fluxes between  $0.64$  and  $3.99 \text{ Jy beam}^{-1}$ , well above the MMB surveys sensitivity of  $0.17 \text{ Jy beam}^{-1}$ , which would suggest that the methanol maser surveys can reveal some high-mass star forming regions that are missed at the sensitivity of ATLASGAL.

A detailed analysis of the correlation and anti-correlation between the ATLASGAL and MMB catalogues and their derived properties is beyond the scope of this paper, but will be presented in a subsequent paper (Urquhart et al., 2012).

## 6.3. Ultra-compact HII regions

We used the unbiased  $5 \text{ GHz}$  VLA radio continuum survey by Becker et al. (1994) to study the association between UCHII regions and submm clumps. In this VLA survey, the Galactic range from  $\ell = 350 - 40^\circ$  and  $|b| < 0.4^\circ$  was covered with the C and CnD configurations, resulting in an angular resolution of  $\sim 4''$ . This radio catalogue contains  $\sim 1300$  sources, 30% of which they tentatively identify as UCHII regions.

Using a search radius of  $20''$  we find in the overlap region of both surveys 170 compact ATLASGAL sources that are positionally coincident with a radio continuum emission ( $\sim 6\%$  of the ATLASGAL sample). Turning to the radio sources we find that 23% of these are associated ATLASGAL sources and are therefore likely to be genuine UCHII regions, which is in reasonable agreement with Becker et al. (1994) initial estimate.

## 6.4. Infrared Dark Clouds

A considerable fraction of submillimetre bright sources appear dark in Spitzer infrared images. Using the Peretto & Fuller (2009) catalogue of infrared dark clouds (IRDC) that is based on the Spitzer GLIMPSE images, we determined the association of ATLASGAL clumps with IRDCs. An association was based on overlap of the source ellipses in the two catalogues. In the part of the Galaxy common to both catalogues, we find that 30% of the IRDCs are associated with ATLASGAL clumps. A similar analysis was recently conducted by Wilcock et al. (2012) in a complementary part of the Galaxy ( $\ell = 300-330^\circ$ ) who determined how many of the IRDCs were seen in the Herschel Hi-GAL  $250/500 \mu\text{m}$  bands. They found a fraction of 38% which is, given the higher mass sensitivity of the Herschel survey, consistent with the ATLASGAL result.

The IRDC peak optical depths are plotted against the peak flux densities measured in ATLASGAL in Fig. 13. Since both quantities are proportional to column density, a correlation is expected. The main uncertainty in the determination of column densities from ATLASGAL data is the dependence of the flux on the dust temperature, which might vary by about a factor 2 (based on ammonia temperatures of ATLASGAL sources,

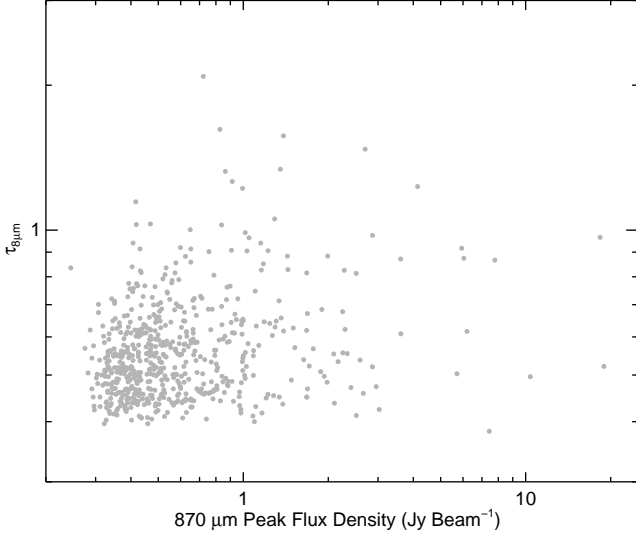


**Fig. 13.** Comparison between peak submm flux densities and  $8\mu\text{m}$  peak optical depths for ATLASGAL sources associated with IRDCs from the Peretto & Fuller (2009) catalogue.

Wienen et al. 2012). Large uncertainties in the determination of IR optical depths result from the estimation of the foreground emission and the subtraction of the background. In addition, for high optical depths, the extinction in the IR will saturate (e.g. Vasyunina et al., 2009). Given these major uncertainties of the latter method, column density estimates by optically thin dust emission in the (sub)millimetre still provide the most reliable method to measure the high column densities towards high-mass star forming clumps.

### 6.5. MSX 21 $\mu\text{m}$ association

To study the mid-infrared properties of the ATLASGAL compact sources in more detail, we extracted the  $21\mu\text{m}$  flux densities from the MSX survey (Price et al., 2001) towards the ATLASGAL peaks. For such an analysis, the MSX data offer two advantages compared to the more sensitive and higher angular resolution data from the Spitzer MIPS GAL  $24\mu\text{m}$  survey (Carey et al. 2009): (i) the spatial resolution of the MSX data ( $18.3''$ ) matches the ATLASGAL resolution extremely well and (ii) the MSX data do not suffer from saturation that MIPS GAL shows towards strong sources, so that the full range of MIR brightnesses can be included in the analysis. This comparison is also more complete than a comparison with the MSX point source catalogue alone, since many ATLASGAL sources are associated with more complex MIR emission not covered in the MSX point source catalogue.

In Fig. 14 we show the correlation of  $870\mu\text{m}$  peak flux density of the ATLASGAL sources and the  $21\mu\text{m}$  MSX fluxes measured at the same position. To remove the contribution from the variable background seen in the  $21\mu\text{m}$  images we have averaged the emission in an annulus centred on the ATLASGAL position with inner and outer radius of  $30''$  and  $120''$ , respectively, and subtracted this from the  $21\mu\text{m}$  flux measured towards the centre of the ATLASGAL sources. The MSX fluxes span a large range and only a loose correlation of increasing MSX with ATLASGAL flux is seen. In fact, a large fraction of the ATLASGAL sources ( $\sim 50\%$ ) show no  $21\mu\text{m}$  emission above the local background level, confirming again that many of the

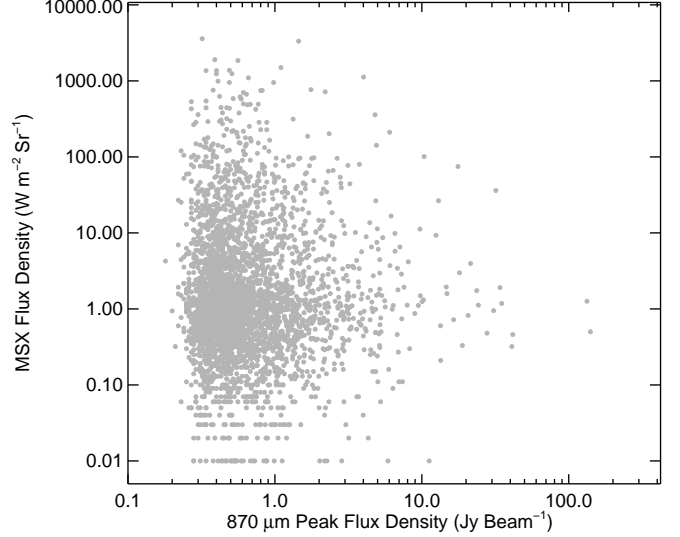


**Fig. 14.** Comparison of peak  $870\mu\text{m}$  fluxes of ATLASGAL sources and the corresponding MSX  $21\mu\text{m}$  fluxes at the same position.

ATLASGAL compact sources do not have embedded or associated luminous infrared sources. However, the fact that approximately half of the ATLASGAL sources have MSX  $21\mu\text{m}$  emission would suggest that the lower limit for the number associated with star formation is closer to 50%. This fraction is significantly higher than found from the straight comparison with the IRAS and MSX PSCs performed in Sect. 6.1. This fraction is likely to increase when the ATLASGAL catalogue is compared with the Spitzer GLIMPSE and MIPS GAL surveys, which will be presented in a future paper.

These background corrected MSX  $21\mu\text{m}$  fluxes can be used to compare the mid-infrared properties of different subsamples ATLASGAL sources. In general terms, the ATLASGAL flux is a measure of the total mass of the clumps while the  $21\mu\text{m}$  MSX flux probes a warm component ( $\sim 100\text{K}$ ) of their spectral energy distributions. Therefore the ratio of both fluxes is a crude measure of the fraction of heated material. We show the histogram of this ratio in Fig. 15 and compare the distribution of this ratio with the corresponding histograms for sources from the RMS survey (Urquhart et al., 2008), both for identified high-mass young stellar objects and HII regions, and with the histogram of this ratio for  $\text{CH}_3\text{OH}$  masers from the MMB survey (Caswell et al., 2010). The peak of the distribution for the RMS YSOs and HII regions is very comparable (green and blue histograms, respectively), and it is clearly offset from the ATLASGAL peak, again showing that with ATLASGAL many clumps with either no star formation or the very early stages of star formation are probed. The  $21\mu\text{m}/870\mu\text{m}$  flux ratio for the methanol masers has a broader distribution (red histogram) which is consistent with covering the flux ratios from both, the bulk of the ATLASGAL and the RMS sources.

## 7. Summary

The ATLASGAL has mapped  $420\text{deg}^2$  of the inner Galaxy at  $870\mu\text{m}$ , which traces thermal emission from dense dust clumps. Here we present a compact source catalogue covering  $153\text{deg}^2$  between Galactic longitude  $330^\circ < \ell < 21^\circ$  and  $|b| < 1.5^\circ$ . The source extraction algorithm SExtractor has been used to iden-

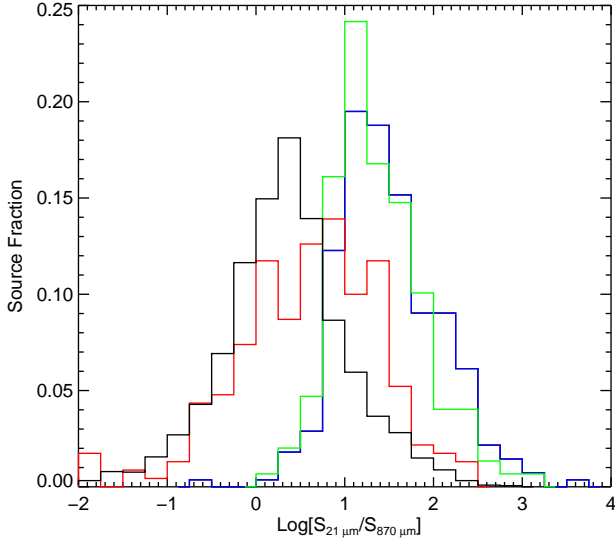


**Fig. 15.** Histogram plots showing the distribution of MSX  $21\ \mu\text{m}$  over ATLASGAL  $870\ \mu\text{m}$  flux ratio for whole ATLASGAL catalogue (black), the methanol masers identified by the MMB survey (red) and UCHII regions and YSOs identified by the RMS survey (coloured blue and green, respectively).

**Table 3.** Summary of associations between ATLASGAL compact sources and infrared and submillimetre surveys.

Catalogue	Coverage within ATLASGAL	N sources
IRAS	Full survey	110
MSX	Full survey	1669
IRAS-MSX	Full survey	645
MMB	$-15^\circ < l < 20^\circ;  b  < 2^\circ$	459
UCHII regions	$10^\circ < l < 21^\circ;  b  < 1^\circ$	170
MSX $21\ \mu\text{m}^*$	Full survey	3410

\* Number of ATLASGAL sources associated with MSX  $21\ \mu\text{m}$  emission above the local background emission (see Sect. 6.5 for details).

tify clumps and determine their parameters. To mitigate the varying r.m.s. noise across the fields we performed the source detection on background subtracted signal-to-noise map, however, the source parameters were determined from the original emission maps. In total 6639 sources have been identified above a  $3\sigma$  threshold ( $\sim 200\ \text{mJy beam}^{-1}$ ) and we find the catalogue is 99% complete above  $6\sigma$ , which corresponds to  $\sim 0.4\ \text{Jy beam}^{-1}$ .

Comparing this catalogue of dense clumps to the MSX and IRAS point source catalogues we find  $\sim 40\%$  are associated with far- and mid-infrared compact sources. The infrared emission likely arises from embedded young stellar objects (YSOs) or UCHII regions and is a strong indication that star formation is currently underway and is in an evolved phase in these clumps. This is supported by the positional correlation of 5 GHz radio continuum emission with approximately 6% of these mid-infrared associated sources. In addition to the mid-infrared and radio associations we find a further  $\sim 500$  clumps are associated with methanol masers ( $\sim 7\%$ ). Methanol masers are thought to trace an earlier evolutionary stage than the mid-infrared emission and have been almost exclusively found to be associated with high-mass star formation regions. A summary with the number of sources with associations among the different surveys is shown in Table 3.

Combined the infrared, radio continuum and methanol maser associated sources make up approximately 50% of the catalogue. These include all of the important evolutionary stages from young deeply embedded protostars identified by methanol masers to mid-infrared bright YSOs and UCHII regions and thus allows for the first time these different samples to be placed into a global framework. However, possibly more intriguing is the other 50% of the sample towards which none of the star formation tracers have been detected as these sources are likely to be in an early stage of evolution. These sources are excellent targets for follow up observation, e.g. in the near future at very high spatial resolution with ALMA.

*Acknowledgements.* We thank the referee for their useful comments and suggestions that have helped to clarify some important points in this paper. This work was partially funded by the ERC Advanced Investigator Grant GLOSTAR (247078) and was partially carried out within the Collaborative Research Council 956, sub-project A6, funded by the Deutsche Forschungsgemeinschaft (DFG). L.B. acknowledges support from CONICYT through project BASAL PFB-06. J. Tackenberg and M. Wien are supported for this research through a stipend from the International Max Planck Research School (IMPRS).

## References

- Aguirre, J. E., Ginsburg, A. G., Dunham, M. K., et al. 2011, *ApJS*, 192, 4
- Becker, R. H., White, R. L., Helfand, D. J., & Zoonematkermani, S. 1994, *ApJS*, 91, 347
- Benjamin, R. A., Churchwell, E., Babler, B. L., et al. 2003, *PASP*, 115, 953
- Bertin, E. & Arnouts, S. 1996, *A&AS*, 117, 393
- Beuther, H., Tackenberg, J., Linz, H., et al. 2012, *ApJ*, 747, 43
- Bonnell, I. A., Vine, S. G., & Bate, M. R. 2004, *MNRAS*, 349, 735
- Carey, S. J., Noriega-Crespo, A., Mizuno, D. R., et al. 2009, *PASP*, 121, 76
- Caswell, J. L., Fuller, G. A., Green, J. A., et al. 2010, *MNRAS*, 404, 1029
- Caswell, J. L., Fuller, G. A., Green, J. A., et al. 2011, *MNRAS*, 417, 1964
- Cyganowski, C. J., Whitney, B. A., Holden, E., et al. 2008, *AJ*, 136, 2391
- Deharveng, L., Schuller, F., Anderson, L. D., et al. 2010, *A&A*, 523, A6
- Di Francesco, J. 2008, in *Bulletin of the American Astronomical Society*, Vol. 40, American Astronomical Society Meeting Abstracts #212, 271
- Dunham, M. K., Rosolowsky, E., Evans, II, N. J., Cyganowski, C., & Urquhart, J. S. 2011, *ApJ*, 741, 110
- Egan, M. P., Price, S. D., Kraemer, K. E., et al. 2003, *VizieR Online Data Catalog*, 5114, 0
- Foster, J. B., Jackson, J. M., Barnes, P. J., et al. 2011, *ApJS*, 197, 25
- Green, J. A., Caswell, J. L., Fuller, G. A., et al. 2009, *MNRAS*, 392, 783
- Green, J. A., Caswell, J. L., Fuller, G. A., et al. 2010, *MNRAS*, 409, 913
- Green, J. A., Caswell, J. L., Fuller, G. A., et al. 2012, *MNRAS*, 420, 3108
- Güsten, R., Booth, R. S., Cesarsky, C., et al. 2006, in *Presented at the Society of Photo-Optical Instrumentation Engineers (SPIE) Conference*, Vol. 6267, Ground-based and Airborne Telescopes. Edited by Stepp, Larry M.. Proceedings of the SPIE, Volume 6267, pp. 626714 (2006).
- Hoare, M. G. & Franco, J. 2007, *ArXiv e-prints*

- Hoare, M. G., Purcell, C. R., Churchwell, E. B., et al. 2012, *PASP*, 124, 939
- Holland, W. S., Robson, E. I., Gear, W. K., et al. 1999, *MNRAS*, 303, 659
- Humphreys, R. M. & Larsen, J. A. 1995, *AJ*, 110, 2183
- Joint Iras Science, W. G. 1994, *VizieR Online Data Catalog*, 2125, 0
- Krumholz, M. R. & Bonnell, I. A. 2007, *ArXiv e-prints*
- Lawrence, A., Warren, S. J., Almaini, O., et al. 2007, *MNRAS*, 379, 1599
- McKee, C. F. & Ostriker, E. C. 2007, *ARA&A*, 45, 565
- McKee, C. F. & Tan, J. C. 2002, *Nature*, 416, 59
- McKee, C. F. & Tan, J. C. 2003, *ApJ*, 585, 850
- Menten, K. M. 1991, *ApJ*, 380, L75
- Molinari, S., Swinyard, B., Bally, J., et al. 2010, *PASP*, 122, 314
- Peretto, N. & Fuller, G. A. 2009, *A&A*, 505, 405
- Planck Collaboration, Ade, P. A. R., Aghanim, N., et al. 2011, *A&A*, 536, A7
- Price, S. D., Egan, M. P., Carey, S. J., Mizuno, D. R., & Kuchar, T. A. 2001, *AJ*, 121, 2819
- Rosolowsky, E., Dunham, M. K., Ginsburg, A., et al. 2010, *ApJS*, 188, 123
- Saito, R. K., Hempel, M., Minniti, D., et al. 2012, *A&A*, 537, A107
- Schuller, F. 2012, *Proceeding of the SPIE conference*, submitted
- Schuller, F., Menten, K. M., Contreras, Y., et al. 2009, *A&A*, 504, 415
- Siringo, G., Kreysa, E., Kovács, A., et al. 2009, *A&A*, 497, 945
- Tackenberg, J., Beuther, H., Henning, T., et al. 2012, *A&A*, 540, A113
- Thompson, M. A., Hatchell, J., Walsh, A. J., MacDonald, G. H., & Millar, T. J. 2006, *A&A*, 453, 1003
- Urquhart, J. S., Hoare, M. G., Lumsden, S. L., Oudmaijer, R. D., & Moore, T. J. T. 2008, in *Astronomical Society of the Pacific Conference Series*, Vol. 387, *Massive Star Formation: Observations Confront Theory*, ed. H. Beuther, H. Linz, & T. Henning, 381
- Urquhart, J. S., Moore, T. J. T., & Schuller, F. 2012, *MNRAS*, Submitted
- Vasyunina, T., Linz, H., Henning, T., et al. 2009, *A&A*, 499, 149
- Wienen, M., Wyrowski, F., Schuller, F., et al. 2012, *A&A*, 544, A146
- Wilcock, L. A., Ward-Thompson, D., Kirk, J. M., et al. 2012, *MNRAS*, 422, 1071
- Wyrowski, F. 2008, in *Astronomical Society of the Pacific Conference Series*, Vol. 387, *Massive Star Formation: Observations Confront Theory*, ed. H. Beuther, H. Linz, & T. Henning, 3